Journal of Advanced College of Engineering and Management

Structure, Dielectric, and Electrical Characterization of 0.9($Bi_{0.5}Na_{0.5}TiO_3$) – 0.1($Bi_{0.5}Sr_{0.25}TiO_3$) (BNT-BST) Solid Solution for Capacitor Applications

[1*]Ram Prasad Aryal, [1]Binod Kumar Bhattarai

[1]*Department of Applied Sciences and Chemical Engineering, Pulchowk Campus, IOE, TU, Nepal*

[*]*Corresponding Author: [*]aryalram@ioe.edu.np*

DOI: 10.3126/jacem.v11i1.84545

Abstract

Eco-friendly 0.9($Bi_{0.5}Na_{0.5}TiO_3$) - 0.1($Bi_{0.5}Sr_{0.25}TiO_3$) (BNT-BST) ceramics were synthesized via the solid-state reaction method. Structural, dielectric, and electrical properties were systematically studied. Rietveld refinement confirmed a pure rhombohedral perovskite structure with R3c symmetry. The dielectric constant peaked at 3456 @1kHz with a high transition temperature ~303ºC. Two dielectric relaxations near 110ºC and 300ºC are attributed to R3c and p4bm PNRs. The dielectric peaks diminished with increasing frequency. Impedance and conductivity analysis indicated NTCR-type semiconducting behavior. Jonshcer's law and frequency exponent trends suggest a conduction mechanism governed by the CBH model. Lastly, the modulus formalism further confirms that the electrical relaxation in the studied sample purely depends on the thermal agitation, as proposed initially by the impedance formalism. The poly-dispersive dielectric behavior is associated with various conduction mechanisms contributed by charge carriers/polarons with short/long-range displacement. The distinctive activation energies estimated from the multifaceted analyses depict that the overall electrical behavior is equally influenced by grains and grain boundaries. This analysis explores the wider applications of modified BNT-based ceramics in the field of electroceramics.

Keywords*—Relaxor ferroelectricity, Rietveld, Nyquist plot, CBH model, Jonscher's power law*

1. INTRODUCTION

Lead-free relaxor ferroelectric ceramics have garnered significant attention due to the increasing demand for environmentally friendly materials in various applications, including high-energy-density capacitors, sensors, actuators, transducers, MEMS devices, filter circuits, phase shifters, and piezoelectric systems. Among these, lead-free piezoelectric and ferroelectric ceramics based on bismuth sodium titanate ($Bi_{0.5}Na_{0.5}TiO_3$, BNT) and barium titanate ($BaTiO_3$, BT) have been extensively studied as promising alternatives to conventional lead-based ceramics, particularly Pb(Zr, Ti)O_3 (PZT), due to rising concerns over lead toxicity and environmental pollution[1].

Ongoing research has focused on developing lead-free piezo/ferroelectric materials with performance characteristics comparable to those of PZT. In this context, BNT has emerged as a leading candidate, exhibiting a rhombohedral perovskite (ABO_3) structure at room temperature, similar to PZT. BNT ceramics possess several advantageous properties such as a high Curie temperature (~320ºC), substantial remnant polarization (P_{rem}=38µC/cm^2), a strong coercive field (E_c=73kV/cm), high maximum polarization (P_{max}>40µC/cm^2), and a moderate piezoelectric coefficient (d33=41pC/N) [2].

Despite these favourable features, pure BNT suffers from drawbacks that limit its practical applications, including high electrical conductivity, which leads to significant leakage currents, a large coercive field that complicates poling, and a high sintering temperature near its melting point. To address these issues, researchers have focused on optimizing BNTs' structural and functional properties by doping at the A-site, B-site, or both, using suitable donor and acceptor ions, and by developing solid solutions near morphotropic phase boundaries (MPBs)

Such strategies aim to tailor phase transitions, enhance relaxor behavior, and improve electromechanical responses. Notably, solid solutions like BNT-BKT have shown promising results. For example, Sakila et al. reported enhanced piezoelectric properties and improved poling behaviour compared to pure BNT. Similarly, Ullah et al. demonstrated that the mixed-phase composition (R3C and P4bm) of BNT-BKT could be transformed into pure R3C phase by incorporating $(Ba_{0.70}\,Sr_{0.30})TiO_3$, thereby optimizing its ferroelectric performance.

To explore the wider applications of BNT-based ceramics, it is imperative to get a deeper understanding of their structural and electrical properties to forecast the system's performance. Therefore, this study aims to analyze the structural, dielectric, and electrical properties of the SBT modified BNT ceramics system. The ionic motion caused by the various factors (temperatures, field frequency) gives rise to the types of conductivity. The AC electrical conductivity is extensively used to identify the nature of ionic motion, types of conduction processes that direct the electrical behavior, and it further forecasts information about crystal defects inherent in it. It is well known that Bismuth and Sodium are volatile and create some defect chemistry during the high-temperature synthesis process. Some defect reactions represented in terms of Kroger-Vink notations are,

$$2Na_{Na}^{x} + O_{O}^{x} \rightarrow V_{O}^{x} + 2V_{Na}^{x} + Na_2O(g)$$

$$V_{O}^{x} + 2V_{Na}^{x} \rightarrow 2V_{Na}^{'} + V_{O}^{\bullet\bullet} + 2h^{\bullet} + 2e^{'}$$

Such vacant oxygen is reabsorbed from the nearby oxygen-rich environment as follows

$$V_O^{\bullet\bullet} + \frac{1}{2}O_2(g) \rightarrow O_O^x + 2h^{\bullet}$$

Similarly for Bi,

$$2Bi_{Bi}^x + 3O_O^x \rightarrow 2V_{Bi}^{'''} + 3V_O^{\bullet\bullet} + Bi_2O_3(g)$$

These collections of point defects and vacancies govern the overall performance of the electrical properties of electroceramics. Several studies on pure BNT and its derivative compounds have been made in the functional electroceramics domain. The development of such point defects and high coercive fields can be alleviated by the introduction of suitable iso/hetero-valent elements or by ABO_3 compounds to the pure BNT host matrix. Such a doping/adding mechanism further enhances the dielectric relaxation through dismantling the long-range FE order (Macrodomain) into dynamic nano domains called polar nano regions (PNRs) [3,4].

Numerous theoretical models, such as the non-overlapping small polaron tunneling (NSPT) model [5], the overlapping large polaron tunneling (OLPT) model [6], the quantum mechanical tunneling (QMT) model [7], and the correlated barrier hopping (CBH) model [8], are prevalent to understand the electrical conduction mechanism of the electroceramics. These models are used to study the constitutive mechanisms of a wide range of materials, such as conductive glasses, polymers, organic/inorganic semiconductors, amorphous semiconductors, and highly defective polycrystalline materials. In general, the AC conductive behaviour is similar to all defective materials, as they depend on the electronic states near the Fermi level. The applied AC field frequency caused the charges to migrate into different defect centers covering long/short-range distances inside the material, following the frequency. Temperature is another crucial factor to alters the AC conductivity, especially in the long-range movement of the charge carriers, as it increases the mobility of the charge carriers and promotes the AC conductivity at elevated temperatures [9–11].

In this research, $Bi_{0.5}Sr_{0.25}TiO_3$ modified BNT perovskite ceramic $0.9[(Bi_{0.5}Na_{0.5}TiO_3) - 0.1(Bi_{0.5}Sr_{0.25}TiO_3)$ (BNT-BST) was prepared using the solid-state reaction method. To the best of my knowledge, this composition has not been investigated in this context to date. The frequency and temperature-dependent real and imaginary parts of the relative permittivity have been studied from room temperature to 500ºC at the frequency range of 1 kHz to 160 kHz. In addition, relaxation time distribution, impedance and modulus spectroscopy, and AC conductivity based on the Cole-Cole plots were carried out to better understand the synthesized samples' electrical conductivity and dielectric relaxation.

2. EXPERIMENTAL

2.1 Synthesis process

Lead-free $0.9[(Bi_{0.5}Na_{0.5}TiO_3) - 0.1(Bi_{0.5}Sr_{0.25}TiO_3)$ (BNT-BST) ceramic was prepared by following the solid-state reaction method. The high-grade chemical powders in the form of oxides/carbonates, namely, Bi_2O_3 (Merck, 99%), Na_2CO_3 (Fisher Sci, 98%), $SrCO_3$ (Hi-Media, 99%), and TiO_2 (Otto, ≥98%), were measured according to the chemical formula with stoichiometric ratios as per the following equation,

$0.25Bi_2O_3+0.225Na_2CO_3+0.0125Sr_2CO_3+TiO_2 \rightarrow 0.9[(Bi_{0.5}Na_{0.5}TiO_3)-0.1(Bi_{0.5}Sr_{0.25}TiO_3 +0.25CO_2$.

These measured powders were then mixed and ground into fine powders with the help of an agate mortar pestle and ethanol as milling media for 10 hours. The slurry was dried for 8 hours at 100˚C in an oven, followed by calcining in a closed crucible at 800˚C for 3 hours in a muffle furnace. The calcined powder is then ground again for 6 hours. The calcined powders were then mixed with 2% PVA as binder, and green pellets having ~10mm in diameter and ~1.10 mm in thickness were formed by applying 10MPa uniaxial pressure at room temperature. The binder contained in the green pellets was then removed by heating it at 600ºC for 4 hours. The green pellets were then closed sintered by adding some bedding powders to minimise the volatile loss of the elements at 1130˚C for 2 hours. The sintered pellet was then ground into fine powders for crystal structure/phase formation identification with the help of the X-ray diffraction technique. For the electrical measurement test, cleaned sintered pellets were coated with silver paste on both sides and kept at 550˚C for 15 minutes to form an electrode.

2.2 Characterization

The identification of the crystal structure and phase formation of the prepared sample was characterized by an X-ray diffractometer (Bruker D2 Phaser- NAST, Khumaltar, Nepal) using CuKα wavelength measured at room temperature, 2θ angle ranging from 20˚-80˚ with a scanning rate of 3˚/min, and 0.02˚ step size. For the confirmation of phase formation and to have deeper insight into the crystal structure, the Rietveld refinement technique was adopted using the FULLPROF suite software. The dielectric and impedance characterization were performed using an impedance analyzer (Keysight E4990A) with a frequency range from 20Hz to 1MHz at room temperature to 500˚C. Bulk density was measured by using Archimedes' principle, and theoretical density and volume were calculated by using refined lattice constants.

3. RESULTS AND DISCUSSION

3.1 X-ray diffraction analysis

The XRD pattern of the synthesized sintered powders of BNT-BST, recorded at room temperature, is shown in Figure 1(a). The XRD pattern reveals the pure

ABO_3 perovskite structure without a noticeable impurity phase within the detection limit of the instrument. A strong intensity peak has been obtained at 2θ ~32˚. For the perovskite structure, the peaks (111) and (200) at 2θ ~39˚- 47º represent the characteristic peaks as they are responsible for the identification of rhombohedral, tetragonal, and cubic crystal symmetry. The splitting of the (111) peak insinuates the presence rhombohedral structure, the (200) peak splitting indicates the tetragonal structure, and the coexistence of rhombohedral and tetragonal takes place for both peaks' splitting. In Figure 1(a), peak indexing has been done based on a hexagonal basis, so the (111) and (200) indexing are not mentioned. Small ignorable impurity peaks are seen near 23º, 30º, and 36º, mainly due to the volatile nature of Bi and Na at high sintering temperatures, which promoted the non-stochiometric phase formation [12,13]. To know the deformation and its stability of a crystal structure, a parameter called the Goldsmith tolerance factor (t) is calculated and given by equation [14]. The value of t varies as ($0.825 < t < 1.059$), and the values closer to unity correspond to a stable structure, and $t \neq 1$ indicates the distorted crystal structure.

$$t = \frac{\left[r_{O}^{2-}+\left(0.5r_{Bi}^{3+}+0.45r_{Na}^{+}+0.05r_{Sr}^{+}\right)\right]}{\sqrt{2}[r_{O}^{2-}+r_{Ti}^{4+}]} \ldots\ldots(1)$$

where r_0 (1.4 Å with coordination number (CN6), r_{Bi} (1.17Å CN12), r_{Na} (1.39 ÅCN12), r_{Sr} (1.44Å CN12), and r_{Ti} (0.605 Å CN6) are the ionic radii of oxygen, bismuth, sodium, Strontium and titanium, respectively [15] [18]. The calculated value of 't' using equation (1) is 0.9460Å, (~1), indicating the distorted stable structure.

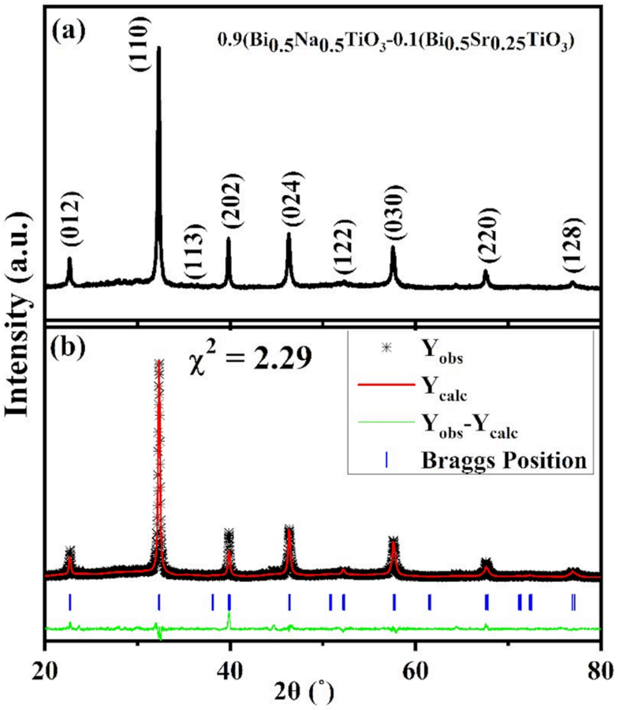

Figure 1: (a) XRD pattern of sintered powder at 1130ºC for 2 hours, (b) corresponding Rietveld refinement plots of BNT-SBT ceramic with R3c symmetry.

3.2 Rietveld refinement analysis

To explore the detailed crystal structure, the Rietveld refinement technique is adopted. The main parameters taken for the refinement process include scale factor, zero shift, lattice parameters, background, half-width parameters, preferred orientations, atomic coordinates, site occupancy, peak shape parameters, B anisotropic, and absorption. The rhombohedral structure with R3C symmetry was used as the initial refinement model [16] as depicted by XRD patterns.

The data fittings began with baseline correction, followed by background adjustment using the linear intercept method, applied between adjustable peak height points. To model the peak profiles influenced by the crystallite size and lattice strains, a pseudo-Voigt function (a combination of Lorentzian and Gaussian components) was utilized. Refinement was performed through ten successive cycles, during which the peak positions errors remained unchanged. The refinement encompassed the above-mentioned parameters. The reliability of the refinement process is demonstrated by the close alignment between the calculated and experimental diffraction patterns as illustrated in Figure 1 (b). Additionally, the moderate value of goodness-of-fit (χ^2) and reduced R-factor values further confirm the validity of the refinement process. The summary of the refined parameters is detailed in Table 1.

Sample	Densities			Lattice constant (Å)	Cell vol. (Å^3)	R-factors (%)			χ^2	Str.	Space group
	Bulk (gm/cm^3)	Theo. (gm/cm^3)	Relative (%)			R_{Wp}	R_p	R_{exp}			
BNT-SBT	5.96	6.17	96.51	a=b=5.5216 (5) c=13.5469(7)	358.17	13.8	9.10	10.33	2.29	Rhombohedral	R3c

Table 1: The summary of the Reitveld refinement parameters.

3.3 Dielectric properties

3.3.1 Temperature-dependent dielectrics

Figure 2(a) illustrates the temperature-dependent behavior of relative permittivity (ε_r) and dielectric loss (TanD) measured from room temperature to 500ºC across a frequency range of 1kHz to 160kHz. As temperature increases, ε_r shows a rising trend, whereas its magnitude decreases with increasing frequency, a typical feature of relaxor ferroelectrics. Also, two prominent dielectric anomaly peaks, a characteristic of BNT-based ceramics, are observed.

The first anomaly, a broad dielectric hump near ~110ºC, corresponds to the depolarization temperature (T_d) and is associated with the thermal evolution as well as coexistence of R3C and P4bm polar nanoregions. The second, more pronounced dielectric peak near ~320ºC, is attributed to the maximum permittivity temperature (T_m) and reflects a transition of P4bm

PNRs into R3C P4bm PNRs. Some studies interpret this as a transition from a ferroelectric to a paraelectric phase beyond ~320ºC [17]. The distinct frequency dispersion observed in both T_d and $T_{m,}$ along with the broad nature of these transitions, confirms the relaxor behavior of the materials. This relaxor character, marked by diffuse phase transitions, is beneficial for various electroceramics applications. Notably, both T_d and Tm peaks shift toward higher temperatures with increasing frequency, and the ε_r curves tend to converge at elevated temperatures and frequencies. This merging is attributed to the disappearance of polar nano regions and dipolar activity beyond the burn temperature, which also causes the vanishing of the T_d peak [18]. The incorporation of Sr^{2+} ions at the A-site induces lattice distortion and local charge fluctuations, leading to the formation of internal electric fields and oxygen vacancies. These factors collectively contribute to the observed dielectric response and phase transition mechanism [19].

The Curie-Weiss law above the Curie temperature T_0, at which the relative permittivity of classical FE materials obeys, is written as [20].

$$\frac{1}{\varepsilon_r} = \frac{T-T_0}{C},\ T > T_0\text{..........}\ (2),\ C\text{: }Curie\ constant.$$

The fitted plot corresponding to equation (2) is shown in Figure 2(d), and the fitted parameters @1kHz are T_0=190.6ºC, $T_{m=}$302.2ºC, T_{cw}=382.6ºC, ε_r =3456, and ΔT_m=T_{cw}-T_m=80.4˚C. Here, T_{cw} corresponds to the temperature at which the ε_r variation starts to deviate to obey from equation (2), and ΔT_m stands for the measurement of the degree of deviation from the Curie-Weiss law. The ΔT_m value indicates a high degree of deviation from the Curie-Weiss law. The Curie constants are estimated above (C_A) and below (C_B) the T_m and found to be 5.13x10^5 K and 3.31x10^5 K, which reveals synthesized ceramic is a displacive-type ferroelectrics. In general, the ratio C_A/C_B = 8 corresponds to a first-order phase transition, and 2 for a second-order phase transition. In this study ratio becomes 1.54, but the existence of a wide gap in T_m-T_0=111.6˚C ≠0 hinders the possibility of a second-order phase transition, confirming the presence of a first-order phase transition [21,22].

The modified Curie-Weiss law is used to analyze the degree of diffuseness or relaxor nature of the synthesized sample. The modified Curie-Weiss law is written as [23],

$$\frac{1}{\varepsilon_r} - \frac{1}{\varepsilon_m} = \frac{\left(T-T_m\right)^{\gamma}}{C}\text{..........}\ (3)$$

where C: Curie-like constant, ε_m: maximum relative permittivity at T_m, T: absolute temperature, and γ: degree of diffuseness coefficient (1≤ γ≤2), where γ =1 for classic FEs, and γ=2 for an ideal relaxor ferroelectric [20]. Figure (b) shows the plot of ln ($1/\varepsilon_r$-$1/\varepsilon_m$) versus ln (T-T_m) based on the eq^n. (8) at 1kHz and the estimated γ value is found to be 1.76 (γ>1) in the studied sample, which reveals the strong relaxation characteristics triggered by adding (Sr^{2+}) into the BNT host matrix. The main reason for the appearance of relaxor nature is mainly due to the breaking of the long-range FE order, domain redirections, and the development of internal stress. This analysis provides the information that relaxor materials do not follow the Curie-Weiss law but follow the modified Curie-Weiss law. Further, it separates the interactions among PNRs in the RFE phase are entirely different from the interactions among dipoles in the paraelectric phase [24].

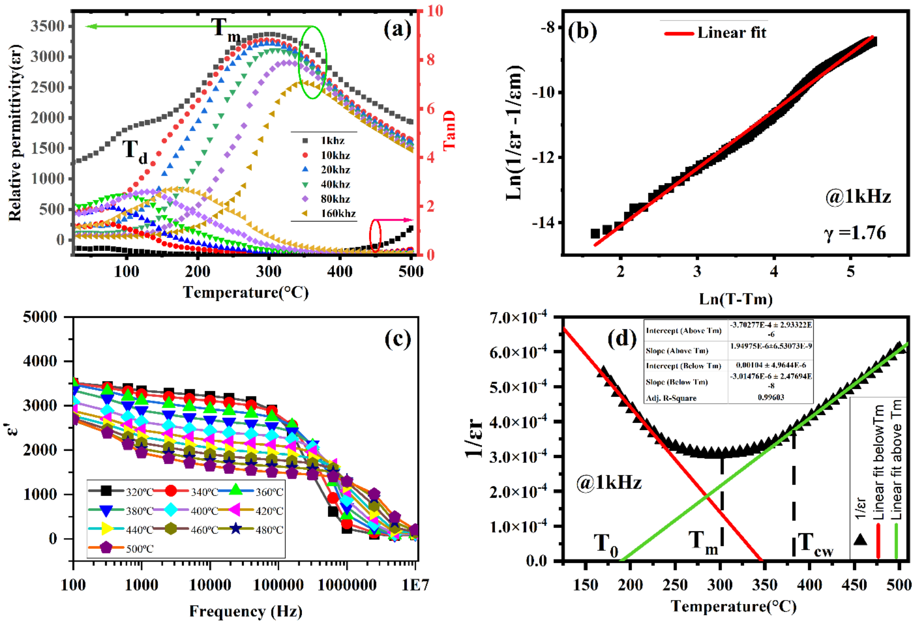

Figure 2: (a) Temperature-dependent relative permittivity (b) plot of modified Cure-Weiss law as of equation (3) (c) Frequency-dependent real part of dielectric constant in the temperature range from 320ºC-500ºC (d) the plot of 1/ε_r vs Temperature

3.3.2 Frequency-dependent dielectrics

The frequency-dependent relative permittivity of the studied sample is plotted in the frequency range from 20Hz to 10^7 Hz and the temperature range from 320ºC to 500ºC as shown in Figure 2(c). The relative permittivity of the polycrystalline ceramics is studied by separating its real and imaginary components as $\varepsilon_r(\omega) = \varepsilon'(\omega)$ (Real) $-j\varepsilon''(\omega)$ (Imaginary/tangent loss, TanD) and expressed in equations (4) and (5) as [9]

$$\epsilon'(\omega) = -\frac{Z''}{\omega . C_0\left(Z'^2+Z''^2\right)} \text{.........} (4)$$

$$\epsilon''(\omega) = \frac{Z'}{\omega . C_0\left(Z'^2+Z''^2\right)} \text{..........} (5)$$

Real part of dielectric characterises the material's energy storage properties, whereas the imaginary part deals with the dielectric loss contributed from the various factors (conduction, heating, high-field frequencies).

The frequency-dependent behaviour of the real part of the dielectric constant (ε′), observed at various temperatures, exhibits distinct characteristics. Initially, at lower frequencies, ε′ values display a slight reduction, followed by a stabilization over a specific frequency range for a constant temperature. Subsequently, a significant decrease in ε′ is observed in higher frequency regions. This behaviour can be considring the contributions of different polarization mechanisms. At lower frequencies, where the condition $\omega\tau<<1$ (with τ denoting the relaxation time) is satisfied, all types of polarization contribute effectively to the dipole polarizations, leading to an almost uniform dielectric constant. As the frequency increases, the relaxation condition shifts to $\omega\tau<1$. Under these circumstances, the dipole oscillating frequency begins to lag behind the applied field frequency, which manifests as a decrease in the dielectric constant values. Furthermore, in the higher frequency regime, specifically when $\omega_m\tau>>1$, only electronic and ionic polarization mechanisms continue to contribute significantly to the dielectric response, resulting in a further reduction of the dielectric constant [25].

According to Maxwell-Wagner interfacial polarization and Koop's phenomenological theory, in polycrystalline ceramics, grains are active at high frequency, while the grain boundaries are agile at low frequency. The oxygen vacancies created during the high-temperature synthesis process induce the space charge polarisation between the electrodes and the material. At low frequencies, these space charges are in phase with the applied field frequencies but lag or do not obey the high-field frequency; as a result, the dielectric varies accordingly. Also, at elevated frequencies, the charge carriers can cross the grain boundaries, increase the conductivity, and reduce the polarisations. The graph further illustrates a rapid decrease in dielectric constant or increase in TanD values at higher temperature, mainly due to the increase in the oxygen vacancies and conductivity due to the thermally activated charge carriers [26,27].

3.3.3 Vogel-Fulcher relation

The Arrhenius model deals with the relaxation process based on thermally activated dipoles at all temperatures above absolute zero and obeys Debye-type relaxations. In contrast, the Vogel-Fulcher model [28] assumes that dipoles are activated after a certain temperature, called the freezing temperature T_f. The Vogel-Fulcher relation is expressed as,

$$f = f_0 exp[- \frac{E_a}{k_B(T_m - T_f)}] ....(6)$$

where f_0: attempt frequency, E_a: activation energy, k_B: Boltzmann's constant, T_d: depolarization temperature, and T_f: freezing temperature.

The temperature corresponding to the maximum dielectric constant (T_m) is frequency dependent, i.e., the maximum dielectric constant peak has been shifted to a higher temperature with frequency. Such behaviour can be explained based on the Vogel-Fulcher model by assuming the activation energy (E_a) of the dipoles and, freezing temperature (T_f) of thermally excited dipoles. The fitted plot according to equation (11) is shown in Figure 3.

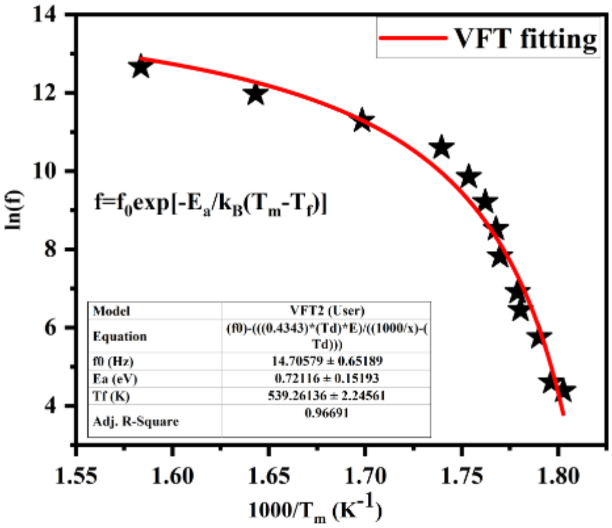

Figure 3: The Vogel-Fulcher relation fittings based on equation (6).

The nonlinear fitting of the experimental data yielded an activation energy of 0.72 eV, a freezing temperature T_f of 539.26 K**,** and an attempt frequency of 5.08×10^{14} Hz. The activation energy E_a reflects the energy barrier that dipolar entities must overcome to respond to the external electric field or how fast the dipoles flip, and its relatively moderate value suggests thermally activated dynamics typical of relaxor ferroelectrics. The high attempt frequency f_0 indicates rapid intrinsic polarization fluctuations in the absence of thermal constraints, consistent with the behavior of nanoscale polar regions. The freezing temperature $T_{f,}$ which marks the onset of dynamic slowing down of these polar nanoregions, lies close to the lower boundary of the dielectric peak temperatures, confirming the presence of glass-like freezing behavior. The excellent fit quality (R^2=0.9669) affirms the applicability of the V-F model and highlights the non-Debye, cooperative relaxation nature intrinsic to relaxor ferroelectric systems [1].

3.4 Impedance spectroscopy analysis

In the polycrystalline ceramics, the behaviours of grains, grain boundaries, and electrode interfaces to the applied electric field greatly influence the impedance and many other electrical properties. Generally, such analyses were performed on the materials used in negative temperature coefficient resistance materials and piezoceramic materials. The complex impedance Z* is described as [29,30],

$$Z^{*} = Z^{'} - jZ^{''} = R_{s} + \frac{1}{j\omega C_{s}} ....(7)$$

where Z', Z", Rs, and C_S are the real and imaginary parts of the impedance, series resistance, and capacitance, respectively.

Figures 4(a) and (b) represent the evolution of real and imaginary parts of the impedance for the synthesized sample in the frequency range from 20Hz to 10^7Hz at various temperatures from 320ºC to 500ºC. As seen from the plot, both Z’ and Z” values are decreasing with increasing frequencies and become stable at higher frequency regions. Further, at high temperature and low frequency, both values are decreasing, indicating the sample behaves as semiconducting materials having a negative temperature coefficient of resistance (NTCR). This decrease in impedances with frequency is attributed to the release of space charge polarisation due to the breaking of charge barriers like grain boundaries [31].

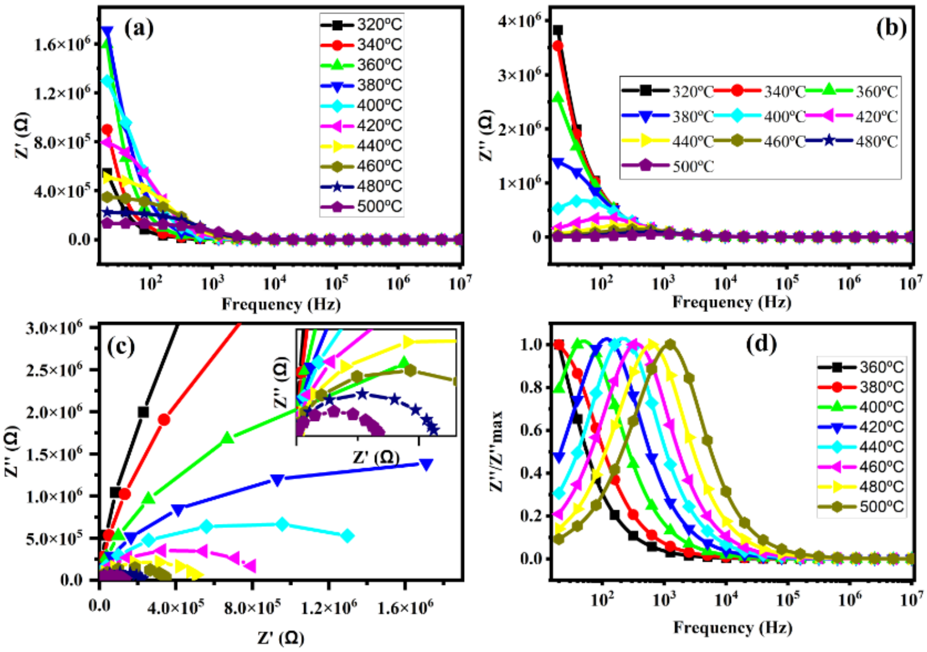

Figure 4: (a) frequency dependent real part of the impedance spectra, (b) frequency dependent imaginary part of the impedance spectra, (c) Nyquist plot, (d) Master impedance plot (Z''/Z'' $_{\max}$ vs. frequency)

The imaginary part (Z'') spectra show some sort of characteristic behavior: i) Z'' $_{\max}$ peak goes on decreasing and shifting towards the higher frequency region with elevated temperatures, and ii) the peaks are broadening asymmetrically with temperatures. That means there is a spread of relaxation time, indicating the presence of temperature-dependent dielectric relaxations in the sample. Overall, the existence of gradually decreasing Z'' $_{\max}$ peaks asymmetrically in the Z'' vs frequency spectrum reveals the existence of dielectric relaxation, and the origin of these peaks is attributed to the matching of the hopping frequency of localized electrons with the applied field frequency. The existence of immobile polarons (electrons, ions) at low temperatures and point defects/vacancies at higher temperatures is primarily responsible for the dielectric relaxations. Each peak associated with a particular temperature has its own relaxation time, and the peak position helps to determine the relaxation frequency $f_{\max}$ and relaxation time using the formulae

$2\pi f_{\max}\tau=1$. The plot of ln (f) and 1000/T has been found to follow the Arrhenius relation in equation (8) [32] shown in Figure 5.

$$f = f_0 \, exp\left(-\frac{E_a}{k_B T}\right) \ldots\ldots\ldots\ldots\ldots (8)$$

where E_a is the activation energy, f_0 is the pre-exponential factor, and k_B is the Boltzmann constant.

From the plot of the relaxation time versus 1000/T, the estimated E_a value is 1.456eV. This estimated value, Ea, suggests that the conduction mechanism in BNT-SBT is of a hopping type.

To have a deeper understanding of the nature of dielectric relaxation, it is worth plotting a Z” vs Z’ plot, also called a Nyquist plot, at temperatures ranging from 320ºC to 500 ºC, as shown in Figure 4(c). As seen from the Nyquist plot, the semicircles with decreasing radii with increasing temperatures and centers that lie below the positive x-axis. This behavior indicates that the dielectric relaxation follows a non-Debye type. The temperature dependence of the radii of Nyquist spectra reveals that the conduction mechanisms are purely governed by thermal processes and proclaims the semiconducting process. The larger value of the diameters at low temperatures manifests that the charge carriers do not acquire sufficient energy to cross the grain boundary and are unable to contribute to the conduction mechanism, and its counterpart at higher temperatures, the diameter decreases [11].

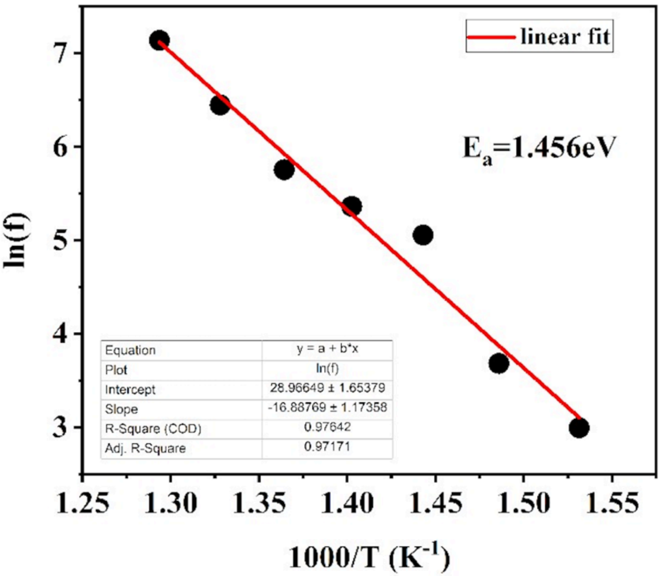

Figure 5: Arrhenius (ln vs Temperature) fitting plot calculated from impedance analysis.

3.5 Conductivity analysis

It is an intrinsic parameter that relates to both the micro- and macroscopic depths of ion mobility and is used to understand the conduction mechanism within the materials, which is influenced by defect states present during the synthesis process. The net electrical conductivity in terms of complex impedance parameters is given by [33]

$$\sigma_{net}(f,T) = \frac{t}{A}\frac{Z'}{Z'^2+Z''^2} \text{...........}(9)$$

where t and A are the thickness and area of the sample.

Figure 6 represents the frequency-dependent AC electrical conductivity of the material measured at various temperatures. The plots reveal two distinct regions, each exhibiting different behaviours concerning frequency and temperature. In the low-frequency region, particularly at lower temperatures, the conductivity remains nearly constant and is attributed to DC conductivity, where charge transport occurs predominantly via a thermally assisted hopping mechanism between localized states. In contrast, at higher frequencies, the conductivity exhibits a clear frequency dispersion, indicative of AC conductivity, which increases with temperature. This behaviour suggests the involvement of thermally activated charge carriers contributing to the overall conduction process, consistent with the semiconducting nature of the dielectric material. The frequency-dependent variation in conductivity can be effectively described using Jonscher's universal law, which characterizes the dynamic response of disordered materials and provides insights into the underlying conduction mechanisms [34].

$$\sigma_{ac}(\omega) = \sigma_{dc} + A\omega^{n} \dots\dots\dots (10)$$

where σ_{ac}: AC conductivity, σ_{dc}: DC conductivity appeared in low frequency, ω: angular frequency, A: temperature-dependent constant, determines the strength of polarizability, n: ($0<n<1$), temperature and frequency dependent exponent that characterizes the degree of interaction between the mobile ions with the surrounding environments. The condition $0<n<1$ insinuates the long-range translational motion of charge carriers, but $n>1$ indicates the restricted or localised motion within the sites, and the literature shows that n(T) can have >1 value [35]. In this work, the n(T) values are obtained from experimental data by fitting the equation (10), and Table 1 summarizes the fitting parameters with fitting plots shown in Figure 7 (a-j)

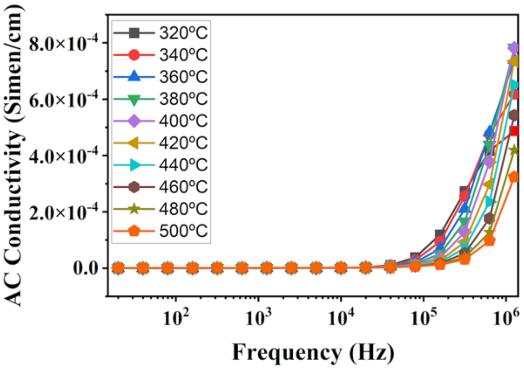

Figure 6: AC conductivity variation with frequency at temperatures ranging from 320ºC-500ºC.

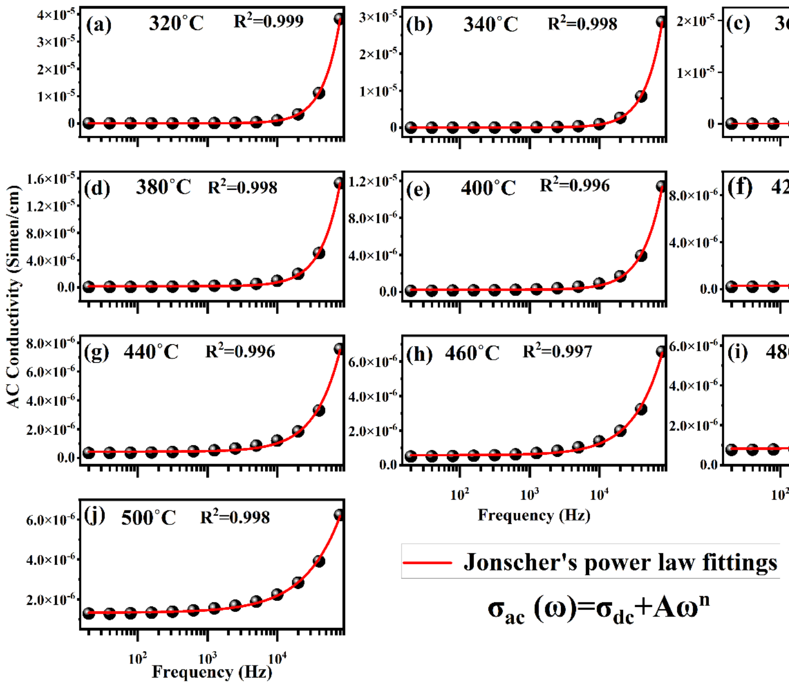

Figure 7: (a) to (j) Jonscher's universal power law fittings based on the equation (10).

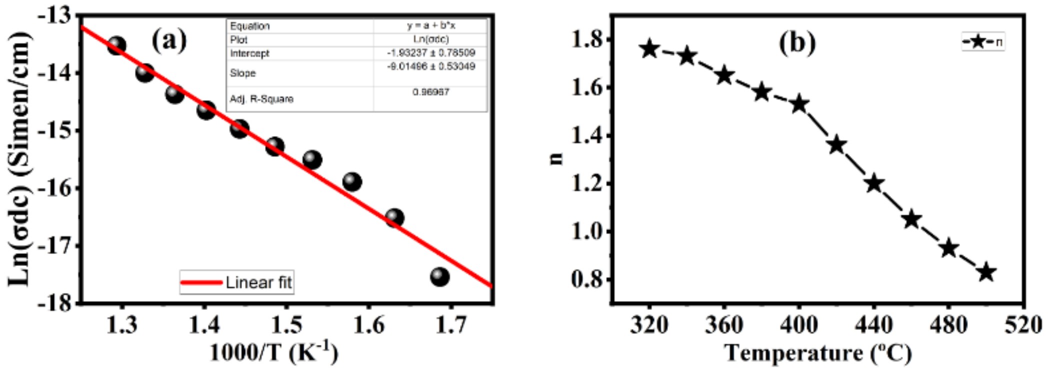

Figure 8: (a) Arrhenius plot of DC conductivity, (b) frequency exponent n(T) plot with temperatures.

Several theoretical models, as mentioned in the introduction, have been proposed to interpret the behavior of the temperature-dependent exponent and the charge transfer mechanism. All these models are based on the combination of the classical charge hopping mechanism and the quantum tunneling effect. In the QMT model, the exponent n is independent of temperature and nearly equal to 0.8; in CBH, n decreases with temperature, indicating that the charge carriers hop across the potential barrier. The exponent n increases with rising temperature in the NSPT model, while in the OLPT model, it depends on both temperature and frequency, initially decreasing to a minimum and then increasing with temperature. Based on the n(t) vs. T curve shown in Figure 8 (b), this study finds that the CBH model effectively describes the conduction mechanism of the charge carriers. As mentioned earlier, the charge carriers hop between sites over the Coulomb potential barrier. In the CBH model, the AC conductivity is given by,

$$\sigma_{AC} = \frac{n_{ph}\pi^2 N N_p \epsilon' \epsilon_0 \omega R_\omega^6}{24} \text{ .... } (11)$$

where n_{ph}: no. of polaron/charge carriers involved in the hopping process, N; density of localized states where carriers remain, N_p: density of localized states where the carriers hop, ε_0: dielectric constant of the free space, ε': dielectric constant of the material, R_ω: hopping distance for conduction.

The conductivity is associated with the hopping mechanism of the polarons created due to charge localization in the adjacent sites of the Columb potential barrier. The activation energy for the DC conduction is estimated by fitting the Arrhenius equation given by equations [36,37].

$$\sigma_{dc} = \sigma_0 . exp\,(-\frac{E_a}{k_B T}) \text{ .... } (12)$$

where $\sigma_{dc:}$ DC conductivity, and it is estimated from the fitting of eq^n. (20) at various temperatures, σ_0: pre-exponential factor, E_a: activation energy responsible for the conduction process, k_B: Boltzmann constant, and T is the absolute temperature. The Arrhenius fitted plot (ln σ_{dc} vs. 1000/T) is shown in Figure 8(a). The estimated value of activation energy (E_a) is found to be 0.777eV, which is closer to the activation energy value for oxygen vacancies (0.5-2eV), which means that oxygen vacancies play a crucial role in the conduction mechanism in the studied sample.

3.6 Modulus spectroscopy analysis

Impedance analysis functions as a resistor, and modulus spectroscopic formalism works as a capacitor in an equivalent RC circuit. In the modulus formalism large density of charge carriers is discarded and considered to be more effective for the relaxation caused by defects in polycrystalline ceramics. In this analysis, the low capacitive value is effective in differentiating the components having the same resistance with several capacitance values. The complex modulus M* is given as [38]

$$M^* = \frac{1}{\epsilon^*} = \frac{1}{(\epsilon' - i\epsilon'')} = \frac{\epsilon'}{\epsilon'^2 + \epsilon''^2} + \frac{i\epsilon''}{\epsilon'^2 + \epsilon''^2} = M' + iM'' \text{ ....} (13)$$

where ε*: complex dielectric constant.

The plots of both real and imaginary parts of complex modulus spectra M* have been plotted with respect to frequency and shown in Figures 9(a) and (b). The sinusoidal variation of M' with frequency shown in Figure 8 (a) suggests the localized movement of charge carriers/ions.

The M' vs frequency plot shown in Figure 8(b) indicates that the sample underwent a thermally activated process as the modulus peaks shifted to higher frequency regions with increasing temperatures. The increase in peak intensity with temperature further suggests that the capacitance caused by relaxation strongly depends on temperature. The shifting of peaks with increasing peak intensity and asymmetric broadening of the peaks refers to the non-Debye type relaxation with a spread of time constants. The master impedance (Z''/Z''_{max}) and modulus (M''/M''_{max}) curves with frequency are shown in Figures 4(d) and 9(c). The asymmetric broadening of these curves also supports the existence of a non-Debye type of relaxation, which is also reported by previous studies [31,34]. The existence of single relaxation peaks at individual temperatures reveals that the relaxation process is caused either by grains or grain boundaries

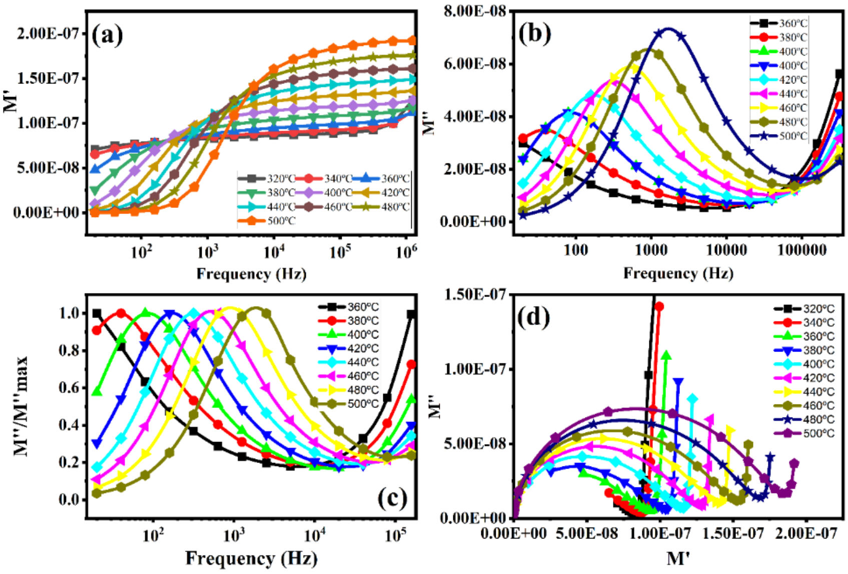

Figure 9: (a) frequency variation of real part of complex modulus spectra at various temperatures, (b) imaginary parts, (c) Master modulus plot (M''/M''_{max}) vs frequency, (d) M'' vs M' curve.

At low frequencies, the M'' peaks become gentler, implying that the electrode effect can be discarded in the modulus formalism. The temperature-dependent relaxation frequency satisfies the relation $\omega_{max}\tau = 1$, plotted and shown in Figure 10, and the plot obeys the Arrhenius law given the equations.

$$f = f_0 \, exp\left(-\frac{E_a}{k_B T}\right) \ldots\ldots\ldots\ldots\ldots (14)$$

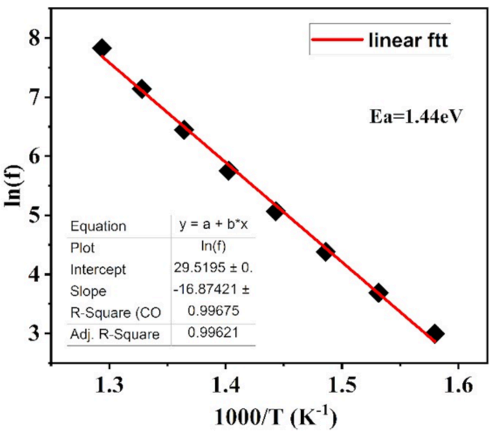

Figure 10: Arrhenius fitting plot of the equation (14) using the data from modulus spectroscopy analysis.

where the symbols have their usual meaning as mentioned above. The estimated activation energy obtained from the linear fit of equation (14) is 1.44 eV. Charge carriers in crystalline materials require some initial energy to move through the material, which is generally provided by heating, known as activation energy. It is observed that the activation energy calculated from impedance, conduction, and the modulus formalism is slightly different, indicating that the movement of charge carriers is hindered by grain boundaries. These energy values are comparable to the activation energy needed for oxygen vacancies to conduct. If all energy values are close to each other, it confirms that both conduction and relaxation mechanisms in the studied sample occur through the same mechanism. The energy values from impedance and conductivity suggest that electronic conduction dominates. [3]

4. CONCLUSION

In this study, the Sr^{2+} modified $Bi_{0.5}Na_{0.5}TiO_3$ (BNT-SBT) lead-free electroceramics were synthesized, and their structure, dielectric, and electrical properties were analyzed thoroughly. The structural analysis showed the rhombohedral structure with R3c space symmetry. The dielectric constant increases with temperature but decreases with frequency and shows strong relaxation behaviour. The maximum dielectric constant reached 3456 at 1kHz, and the transition temperature became ~303ºC. The dielectric relaxation behaviour is attributed to the dynamics of thermally activated PNRs below the burn temperature. The complex impedance spectra suggest that the conduction mechanism is purely dependent on the density of the electronic states contributed from the ionization of oxygen vacancies. Conductivity analysis shows that the conductivity spectra obey Jonscher’s power law, and the frequency exponent confirms that the conduction phenomena are well described with the help of the CBH model. Finally, the modulus spectrum analysis revealed that the conduction relaxation is purely due to thermally activated processes. The discussion on the basis of this work concludes that all the relaxation processes are implicitly associated with the creation and ionisation of oxygen vacancies. The master modulus curve reveals that the relaxation is of a non-Debye type. The combination of high relative permittivity, large impedance, and low conductivity enhances its practical applicability, particularly in pulse power energy storage and phase-shifter capacitors.

ACKNOWLEDGEMENT

The authors sincerely thank [Late] Bhadra Prasad Pokhrel for his valuable guidance during the laboratory work. Financial support from the University Grants Commission (UGC), Bhaktapur, Nepal (Grant No. Ph.D. 77/78-ST-16), is gratefully acknowledged. The author also extends appreciation to SMST, IIT (BHU), India, for providing the facilities required for dielectric measurements.

REFERENCES

[1] R.P. Aryal, B.K. Bhattarai, A.K. Singh, High dielectric energy storage performance of $Bi(Ni_{0.5}Zr_{0.5})O_3$ substituted $Bi_{0.5}(Na_{0.70}K_{0.30})_{0.5}TiO_3$-based relaxor ferroelectric ceramics, Mater Today Commun 46 (2025) 112885. https://doi.org/10.1016/j.mtcomm.2025.112885.

[2] P. Jaita, S. Manotham, P. Butnoi, R. Sanjoom, P. Arkornsakul, D.R. Sweatman, C. Kruea-In, T. Tunkasiri, The mechanical and electrical properties of modified-BNKT lead-free ceramics, Integrated Ferroelectrics 187 (2018) 147–155. https://doi.org/10.1080/10584587.2018.1444888.

[3] L. Liu, H. Fan, L. Fang, X. Chen, H. Dammak, M.P. Thi, Effects of Na/K evaporation on electrical properties and intrinsic defects in $Na_{0.5}K_{0.5}NbO_3$ ceramics, Mater Chem Phys 117 (2009) 138–141. https://doi.org/10.1016/j.matchemphys.2009.05.024.

[4] L. Yang, X. Chao, P. Liang, L. Wei, Z. Yang, Electrical properties and high-temperature dielectric relaxation behaviors of $Na_xBi_{(2-x)/3}Cu_3Ti_4O_{12}$ ceramics, Mater Res Bull 64 (2015) 216–222. https://doi.org/10.1016/j.materresbull.2014.12.060.

[5] M. Dult, R.S. Kundu, S. Murugavel, R. Punia, N. Kishore, Conduction mechanism in bismuth silicate glasses containing titanium, Physica B Condens Matter 452 (2014) 102–107. https://doi.org/10.1016/j.physb.2014.07.004.

[6] A.R. Long, Frequency-dependent loss in amorphous semiconductors, Adv Phys 31 (1982) 553–637. https://doi.org/10.1080/00018738200101418.

[7] I.G. Austin, N.F. Mott, Polarons in crystalline and non-crystalline materials, Adv Phys 18 (1969) 41–102. https://doi.org/10.1080/00018736900101267.

[8] M. Krimi, K. Karoui, J.J. Suñol, A. Ben Rhaiem, Phase transition, impedance spectroscopy and conduction mechanism of $Li_{0.5}$ $Na_{1.5}WO_4$ material, Physica E Low Dimens Syst Nanostruct 102 (2018) 137–145. https://doi.org/10.1016/j.physe.2018.04.032.

[9] U. Akgul, Z. Ergin, M. Sekerci, Y. Atici, AC conductivity and dielectric behavior of, Vacuum 82 (2007) 340–345. https://doi.org/10.1016/j.vacuum.2007.05.001.

[10] Y. Ben Taher, N. Moutia, A. Oueslati, M. Gargouri, Electrical properties, conduction mechanism and modulus of diphosphate compounds, RSC Adv 6 (2016) 39750–39757. https://doi.org/10.1039/C6RA05220G.

[11] W. Ncib, A. Ben Jazia Kharrat, M. Saadi, K. Khirouni, N. Chniba-Boudjada, W. Boujelben, Structural, AC conductivity, conduction mechanism and dielectric properties of $La_{0.62}Eu_{0.05}Ba_{0.33}Mn_{0.85}Fe_{0.15}O_3$ ceramic compound, Journal of Materials Science: Materials in Electronics 30 (2019) 18391–18404. https://doi.org/10.1007/s10854-019-02193-0.

[12] L. Ramajo, J. Camargo, F. Rubio-Marcos, M. Castro, Influences of secondary phases on ferroelectric properties of Bi(Na, K)TiO3 ceramics, Ceram Int 41 (2015) 5380–5386. https://doi.org/10.1016/j.ceramint.2014.12.100.

[13] J. Camargo, A. Prado Espinosa, L. Ramajo, M. Castro, Influence of the sintering process on ferroelectric properties of Bi0.5(Na0.8K0.2)0.5TiO3 lead-free piezoelectric ceramics, Journal of Materials Science: Materials in Electronics 29 (2018) 5427–5432. https://doi.org/10.1007/s10854-017-8508-8.

[14] T. Sato, S. Takagi, S. Deledda, B.C. Hauback, S. Orimo, Extending the applicability of the Goldschmidt tolerance factor to arbitrary ionic compounds, Sci Rep 6 (2016) 23592. https://doi.org/10.1038/srep23592.

[15] R.D. Shannon, Revised effective ionic radii and systematic studies of interatomic distances in halides and chalcogenides, Acta Crystallographica Section A 32 (1976) 751–767. https://doi.org/10.1107/S0567739476001551.

[16] G.O. Jones, J. Kreisel, P.A. Thomas, A structural study of the $(Na_{1-x}K_x)_{0.5}Bi_{0.5}TiO_3$ perovskite series as a function of substitution (x) and temperature, Powder Diffr 17 (2002) 301–319. https://doi.org/10.1154/1.1505047.

[17] P. Butnoi, S. Manotham, P. Jaita, K. Pengpat, S. Eitssayeam, T. Tunkasiri, G. Rujijanagul, Effects of processing parameters on phase transition and electrical properties of lead-free BNKT piezoelectric ceramics, Ferroelectrics 511 (2017) 42–51. https://doi.org/10.1080/00150193.2017.1333364.

[18] W.-Q. Luo, Z.-Y. Shen, Y.-Y. Yu, F.-S. Song, Z.-M. Wang, Y.-M. Li, Structure and dielectric properties of NBT-xBT-ST lead-free ceramics for energy storage, J Adv Dielectr 08 (2018) 1820004. https://doi.org/10.1142/S2010135X18200047.

[19] B. Kaur, AC Impedance Spectroscopy, Conductivity and Optical Studies of Sr doped Bismuth Ferrite Nanocomposites, Int J Electrochem Sci (2016) 4120–4135. https://doi.org/10.20964/110353.

[20] B.C. Das, M.A. Matin, A.K.M.A. Hossain, Rietveld refinement structure, electric, dielectric and ferroelectric properties of lead-free $Ba_{0.985}Sr_{0.015}Zr_{0.10}Ti_{0.90}O_3$ ceramics, Journal of Materials Science: Materials in Electronics 32 (2021) 4916–4936. https://doi.org/10.1007/s10854-020-05231-4.

[21] G. Gong, G. Zerihun, Y. Fang, S. Huang, C. Yin, S. Yuan, Relaxor Behavior and Large Room‐Temperature Polarization of Ferroelectric $Sr_4CaBiTi_3$ Nb_7O_{30} Ceramics, Journal of the American Ceramic Society 98 (2015) 109–113. https://doi.org/10.1111/jace.13256.

[22] G. Gong, Y. Wang, D. Liu, Y. Su, G. Zerihun, Y. Qiu, S. Yuan, Lead-free relaxor ferroelectric ceramics $Sr_{4+x}Ca_{1-x}BiTi_3Nb_7O_{30}$ with tunable transition temperature, J Mater Sci 51 (2016) 7336–7342. https://doi.org/10.1007/s10853-016-0018-1.

[23] L.N. Shi, Z.H. Ren, A. Jain, R.H. Jin, S.S. Jiang, H.Z. Zhou, F.G. Chen, Y.G. Wang, Enhanced energy storage performance achieved in $Na_{0.5}Bi_{0.5}TiO_3$–$Sr_{0.7}Bi_{0.2}TiO_3$ ceramics via domain structure and bandgap width tuning, Ceram Int 49 (2023) 12822–12831. https://doi.org/10.1016/j.ceramint.2022.12.149.

[24] A. Singha, S. Praharaj, S.K. Rout, D. Rout, Composition dependent crossover from ferroelectric to relaxor-ferroelectric in NBT-ST-KNN ceramics, Current Applied Physics 36 (2022) 160–170. https://doi.org/10.1016/j.cap.2022.02.002.

[25] R.P. Aryal, Dielectric relaxation, AC conductivity, and modulus spectroscopic behavior of eco-friendly BNKLT ceramics, Phase Transitions (2025) 1–24. https://doi.org/10.1080/01411594.2025.2520332.

[26] P. Nayak, T. Badapanda, A.K. Singh, S. Panigrahi, An approach for correlating the structural and electrical properties of Zr^{4+}-modified $SrBi_4Ti_4O_{15}$/SBT ceramic, RSC Adv 7 (2017) 16319–16331. https://doi.org/10.1039/C7RA00366H.

[27] R.P. Parida, B. Parida, R.K. Bhuyan, S.K. Parida, Structural, mechanical and electric properties of La doped BNT-BFO perovskite ceramics, Ferroelectrics 571 (2021) 162–174. https://doi.org/10.1080/00150193.2020.1853751.

[28] A.A. Bokov, M.A. Leshchenko, M.A. Malitskaya, I.P. Raevski, Dielectric spectra and Vogel-Fulcher scaling in $Pb(In_{0.5}Nb_{0.5})O_3$ relaxor ferroelectric, Journal of Physics: Condensed Matter 11 (1999) 4899–4911. https://doi.org/10.1088/0953-8984/11/25/309.

[29] C.A. Angell, Dynamic processes in ionic glasses, Chem Rev 90 (1990) 523–542. https://doi.org/10.1021/cr00101a006.

[30] Y. Qiu, Z. Yu, X. Wang, X. Qiao, Dielectric, ferroelectric, piezoelectric properties, and conduction behavior of $(Bi_{0.5}Na_{0.5})_{0.94+x}Ba_{0.06}TiO_3$ ceramics, Journal of Materials Science: Materials in Electronics 35 (2024) 621. https://doi.org/10.1007/s10854-024-12387-w.

[31] K.Ch. Varada Rajulu, B. Tilak, K. Sambasiva Rao, Impedance spectroscopy study of BNKLT polycrystalline ceramic, Applied Physics A 106 (2012) 533–543. https://doi.org/10.1007/s00339-011-6631-6.

[32] Kh. Dhahri, Dielectric, ac conductivity and modulus studies of sol–gel BaZrO 2.9 compound, Phase Transitions 93 (2020) 802–812. https://doi.org/10.1080/01411594.2020.1789917.

[33] M. Jebli, Ch. Rayssi, J. Dhahri, K. Khirouni, Investigation of electrical properties and conduction mechanism using CBH model of $Ba_{0.97}La_{0.02}Ti_{1-x}Nb_{4x/5}O_3$ ($x = 0.00$ and 0.02) compounds, Applied Physics A 126 (2020) 109. https://doi.org/10.1007/s00339-020-3298-x.

[34] Ch.K.V. Rajulu, S. Ramesh, T.A. Babu, V. Raghavendra, D. Gangadharudu, K.S. Rao, Structural and modulus spectroscopy studies of $Bi_{0.5}(Na_{0.8}K_{0.2})_{0.5}TiO_3$ nano-polycrystalline ceramic, Journal of the Australian Ceramic Society 58 (2022) 83–91. https://doi.org/10.1007/s41779-021-00666-2.

[35] A.N. Papathanassiou, I. Sakellis, J. Grammatikakis, Universal frequency-dependent ac conductivity of conducting polymer networks, Appl Phys Lett 91 (2007). https://doi.org/10.1063/1.2779255.

[36] K. Shimakawa, Glasses: Polaron Transport, in: Encyclopedia of Materials: Science and Technology, Elsevier, (2001) 3579–3581. https://doi.org/10.1016/B0-08-043152-6/00637-9.

[37] A.K. Roy, A. Singh, K. Kumari, K. Amar Nath, A. Prasad, K. Prasad, Electrical Properties and AC Conductivity of $(Bi_{0.5}Na_{0.5})_{0.94}Ba_{0.06}TiO_3$ Ceramic, ISRN Ceramics 2012 (2012) 1–10. https://doi.org/10.5402/2012/854831.

[38] R. Tripathi, A. Kumar, C. Bharti, T.P. Sinha, Dielectric relaxation of ZnO nanostructure synthesized by soft chemical method, Current Applied Physics 10 (2010) 676–681. https://doi.org/10.1016/j.cap.2009.08.015.